Journal of Medicinal Chemistry

Article

Fragment-Based Ligand Design of Novel Potent Inhibitors of Tankyrases

E. Andreas Larsson,*[,†,∥] Anna Jansson,[†,∥] Fui Mee Ng,[§] Siew Wen Then,[§] Resmi Panicker,[†] Boping Liu,[§] Kanda Sangthongpitag,[§] Vishal Pendharkar,[§] Shi Jing Tai,[§] Jeffrey Hill,[§] Chen Dan,[†] Soo Yei Ho,[§] Wei Wen Cheong,[§] Anders Poulsen,[§] Stephanie Blanchard,[§] Grace Ruiting Lin,[§] Jenefer Alam,[§] Thomas H. Keller,[§] and Pär Nordlund*[,†,‡]

[†]School of Biological Sciences, Nanyang Technological University, Lab 07-01, 61 Biopolis Drive (Proteos), Singapore 138673

[‡]Department of Medical Biochemistry and Biophysics, Karolinska Institute, Scheeles väg 2, SE-171 77 Stockholm, Sweden

[§]Experimental Therapeutics Centre, 31 Biopolis Way, Nanos Level 3, Singapore 138669

Supporting Information

ABSTRACT: Tankyrases constitute potential drug targets for cancer and myelin-degrading diseases. We have applied a structure- and biophysics-driven fragment-based ligand design strategy to discover a novel family of potent inhibitors for human tankyrases. Biophysical screening based on a thermal shift assay identified highly efficient fragments binding in the nicotinamide-binding site, a local hot spot for fragment binding. Evolution of the fragment hit 4-methyl-1,2-dihydroquinolin-2-one (**2**) along its 7-vector yields dramatic affinity improvements in the first cycle of expansion. A crystal structure of 7-(2-fluorophenyl)-4-methylquinolin-2(1*H*)-one (**11**) reveals that the nonplanar compound extends with its fluorine atom into a pocket, which coincides with a region of the active site where structural differences are seen between tankyrases and other poly(ADP-ribose) polymerase (PARP) family members. A further cycle of optimization yielded compounds with affinities and IC_{50} values in the low nanomolar range and with good solubility, PARP selectivity, and ligand efficiency.

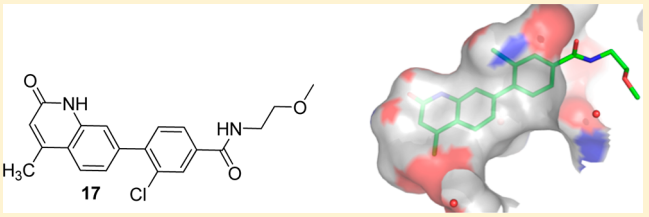

INTRODUCTION

Tankyrase (TNKS) in its two isoforms, TNKS1 and TNKS2, is a subset of the PARP family of proteins, which constitute potential drug targets for cancer and myelin-degrading diseases.[1] Functionally, TNKSs as other PARPs are poly-ADP-ribosylating enzymes that transfer ADP-ribose moieties from NAD+ to a variety of substrates.[2] Poly-ADP-ribosylation affects the protein substrates in different ways, but most often by reducing the activity of the modified protein, as in the case of TNKS modification of TRF1.[3] Other members of the PARP family have been identified as good interference points for drug discovery,[4] perhaps most notably to target DNA repair in BRCA-driven cancers. TNKSs have been implicated in a diverse range of functions, such as regulation of telomeric length, regulation of the Wnt signaling pathway, control of the mitotic checkpoint, and mediation of insulin-stimulated glucose uptake.[5] TNKS1 and TNKS2 have emerged as potential cancer targets on the basis of the observation that inhibition of TNKS acts as a negative regulator for the Wnt/β-catenin pathway in colon cancer cells by stabilizing Axin.[6] Recent studies using selective inhibitors corroborate the hypothesis that it is the inhibition of TNKSs and not off-target effects on other PARPs that is responsible for the observed effect.[7] Although these compounds are not very potent, they prove the point that the selectivity profile is an important aspect in the development of TNKS inhibitors. When inhibited, TNKS can no longer perform poly-ADP-ribosylation on its substrates, including Axin. This stabilizes Axin, and the Axin turnover is shifted, which leads to a negative regulation of the Wnt/β-catenin pathway.[6] Known inhibitors or inhibitor series of TNKSs such as **1** (XAV939)[6] (Figure 1), 1,1‴,2,2‴-tetrahydrotrispiro-[indole-3,2′:5′,5″-bis([1,3]dioxane)-2″,3‴-indole]-2,2‴-dione (JW67), and 4-[4-(4-methoxyphenyl)-5-({[3-(4-methylphenyl)-1,2,4-oxadiazol-5-yl]methyl}sulfanyl)-4*H*-1,2,4-triazol-3-yl]-pyridine (JW74),[8] as well as other compounds,[9,10] originated or were derived from compounds found in cell-based HTS (high-throughput screening) screens targeting Wnt signaling. TNKS

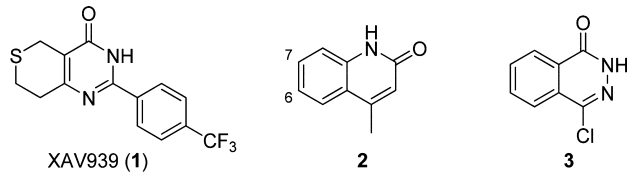

Figure 1. Structure of **1** and fragment hits **2** and **3**. The 6- and 7-vectors are indicated for compound **2**.

Received: February 9, 2013
Published: May 14, 2013

   dx.doi.org/10.1021/jm400211f | *J. Med. Chem.* 2013, 56, 4497−4508

Scheme 1. Synthesis of Compounds 8−15[a]

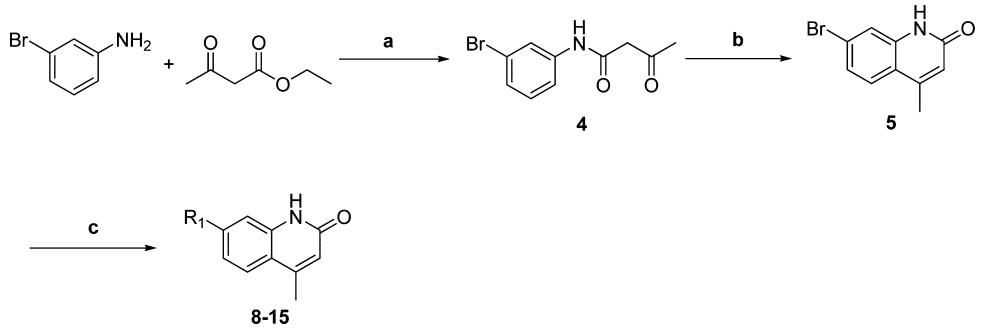

[a]Reagents and conditions: (a) toluene, reflux; (b) concentrated H_2SO_4, 120 °C; (c) $Pd(PPh_3)_4$, arylboronic acid, K_2CO_3, 4:1 dioxane/water, reflux.

Scheme 2. Synthetic Route to Compounds 16 and 17[a]

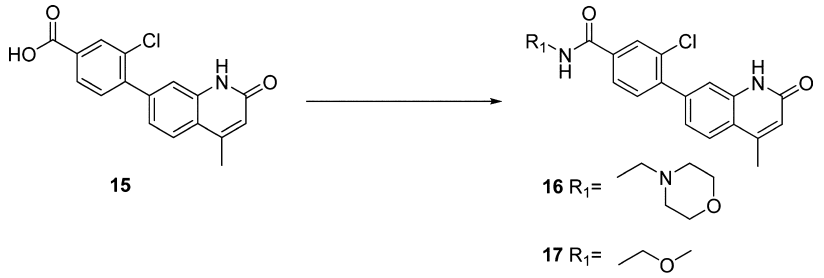

[a]Reagents and conditions: HATU, Hunig's base, dichloromethane.

was only later identified as the molecular target of the compounds.

In this study, we specifically targeted the catalytic PARP domain of TNKS2 directly using a battery of biophysical methods. Fragment hits, discovered by a thermal shift assay, were optimized into high-affinity inhibitors of TNKS2. The expansion of the fragment hits to potent TNKS2 inhibitors was guided by high-resolution structures of protein−ligand complexes, and compounds were characterized using both biophysical and activity assays, and TNKS2/PARP selectivity was evaluated for representative compounds. Structures of the more potent late-stage compounds were also used for the introduction of solubilizing groups in noninterfering positions to provide compounds with better physical properties.

Synthesis. The synthesis of the TNKS inhibitors is described in Scheme 1. 3-Bromoaniline was reacted with ethyl acetoacetate in refluxing toluene, affording the *β*-ketoamide (**4**), which was cyclized in concentrated sulfuric acid to quinolone-2-one (**5**). The substituents on C7 of **5** were introduced via Suzuki coupling (Scheme 1). Similarly, C6-substituted analogues were prepared from commercially available 6-bromo-4-methylquinoline-2(1*H*)-one. Solubilizing groups were introduced by *O*-(7-azabenzotriazol-1-yl)-*N*,*N*,*N*′,*N*′-tetramethyluronium hexafluorophosphate (HATU)-mediated amide synthesis (Scheme 2).

RESULTS

Binding of NAD+ is a central feature for all PARP proteins as NAD+ acts as a donor of ADP-ribose moieties onto various substrates with simultaneous release of nicotinamide. Structurally, the nicotinamide moiety is anchored by three key polar interactions between the nicotinamide amide group and residues Gly1032 and Ser1068 in TNKS2 (Figure 2a). PARPs bind the nicotinamide moiety with high efficiency, and it is perhaps not surprising that this is an affinity hot spot where most PARP inhibitors are anchored.[11] An exception is the newly discovered class of inhibitors that instead interact with the D-loop and induce conformational changes.[8,12]

Fragment Screening. In this study we have used a fragment-based ligand design (FBLD) strategy to identify novel inhibitors for TNKS2. Our strategy is based on the extensive use of biophysical screening to identify leads for crystallography and further evolution into mature compounds. A thermal shift assay (TSA)-based strategy using differential scanning fluorometry (DSF)[13] was used for initial fragment screening of a 500 compound fragment library and hit characterization and as one of the main metrics for the lead optimization process. DSF screening was performed at a compound concentration of 1 mM. Positives were validated to "hits" internally by checking for dose-dependent response, typically tested over a concentration range from 5 to 4000 μM. From our experience, collecting data over a wide range of concentrations is important to remove oddly behaving compounds from the hit list. It also assists in revealing other concentration-dependent effects such as insolubility or aggregation. This method was used for the characterization of all compounds in this paper (see Figures S3 and S4, Supporting Information).

Interpretation of the screening data was complicated by the fact that the melting profile of TNKS2 did not exhibit a clear sigmoidal transition, but rather a two/multiple-state transition (Figure 2c). Assay validation experiments using known TNKS/PARP inhibitors showed which part of the curve (explicitly the last transition) was stabilized upon binding. Although the nonsigmoidal melting behavior does not cause any real trouble for characterization compounds with large thermal shifts, it does significantly complicate the use of numerical selection (and the fitting of T_m) for weakly stabilizing fragments. We

dx.doi.org/10.1021/jm400211f | J. Med. Chem. 2013, 56, 4497−4508

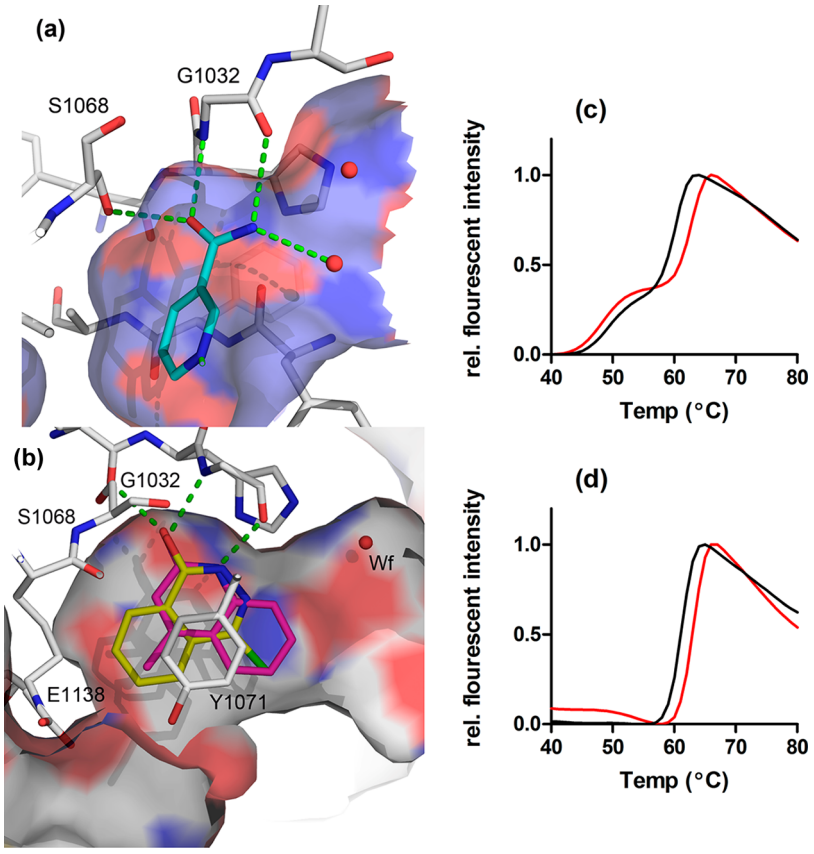

Figure 2. (a) Key active site residues (polar interactions with Gly1032 and Ser1068) for binding of nicotinamide in TNKS2 (PDB 3U9H). (b) Aligned overlay of the crystal structure of the protein–ligand complex of **2** (magenta) and **3** (yellow) in TNKS2 showing the hydrogen bonding to Ser1068 and Gly1032 as well as a surface representation of the pocket. Comparison of thermal shift data for TNKS2 (c) and chymotrypsin-treated TNKS2 (d). The DMSO control is depicted in black and runs in the presence of **2** (here shown at a concentration of 4 mM to better visualize the stabilization vs the DMSO control) in red.

found it much more reliable to manually inspect all transitions and to avoid contaminating the hit set with large numbers of false positives. We also found that adding chymotrypsin to the DSF experiment greatly simplified the interpretation by removing the first, nonreporting transition altogether (Figure 2d).

Two compounds, 4-methyl-1,2-dihydroquinolin-2-one (**2**) and 4-chloro-1,2-dihydrophthalazin-1-one (**3**) (Figure 1), gave melting curves distinct from that of the DMSO control, stabilizing TNKS2 by 1.1 and 1.3 °C, respectively, at 1 mM. Further analysis and triage established that these two compounds also showed a dose-dependent stabilization. Cleaner looking data with in situ trypsination of TNKS2 (see the Experimental Section for details) in combination with concentration-dependent stabilization of T_m were also collected, further strengthening the validation (Figure 2d). These compounds were further characterized with a PARsylation-based activity assay (Table 1) and crystallography (Figure 2b).

Typically, ligand efficiency[14] (LE; in this work expressed as pIC_{50}/HA) is the preferred metric for ranking and prioritization of hits for follow-up. We decided to optimize a scaffold based on compound **2** despite the slightly lower LE compared to that of **3** (0.41 and 0.45, respectively), the main reason being that **2** possesses better geometrical vectors for expansion. In addition, the binding mode of **2** has less overlap with **1** and hence could provide more novel compounds.

First Round of Expansion. Analysis of the crystal structure of the two fragments bound to TNKS2 showed hydrogen bonding to Ser1068 and Gly1032 also seen in nicotinamide binding and the stacking of the compound to Tyr1071. This suggested that there were two major areas of fragment **2** that could be further optimized. One of these is the methyl group of **2** at the 4-position, which is roughly in the same position as the cyclic thioether moiety of **1**, protruding down toward the catalytic glutamate (Glu1138) (Figure 2b). Substitution at the 4-position is very important, as the analogue lacking the methyl group (compound **6**, Table 1) is inactive in all our assays. A small set of analogues with small variations/extensions of the methyl group were prepared and purchased. However, these compounds did not show any improvements from **2** in TSA or activity assays (see Table S3, Supporting Information).

The other interesting position for expansion is through the 7-position of **2**, which points toward the extended pocket responsible for adenosine binding (Figure 2b). It was immediately apparent from TSA data that compounds extended in the 7-position induced significantly more stabilization of TNKS2 than **2**. Compound **7** (prepared as a control for the structure-based expansion hypothesis), which instead extends at the 6-position, showed no stabilizations in the TSA assay, most likely since extensions in this vector clash into the protein (Figure 2b).

The expansion strategy was based on Suzuki couplings using **5** and a set of arylboronic acids. Using this strategy, a small set of compounds were assembled. The most interesting was

dx.doi.org/10.1021/jm400211f | J. Med. Chem. 2013, 56, 4497–4508

Table 1. Biophysical, Structural, and Activity Data on Fragment Hits and Key Intermediates for TNKS2

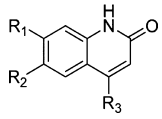

Cpd	R_1	R_2	R_3	IC_{50} (μM)[a]	DSF ΔT_m	K_d (μM)	LE[g]	Xray structure
2	H	H	Me	12	1.1 °C[c]	-	0.41	3W61
6	H	H	H	>20	-	-	-	-
7	H	Ph	Me	>20	0.6 °C[d]	-	-	-
8	Ph	H	Me	0.18	3.2 °C[d]	0.9[e]	0.37	no density[h]
9		H	Me	0.31	3.1 °C[d]	-	0.34	-
10		H	Me	0.15	4.4 °C[d]		0.36	-
11		H	Me	0.052	5.1 °C[d]	0.28[f]	0.38	4IUE
12		H	Me	0.009[b]	6.3 °C[d]	0.057[f]	-	no density[h]
13		H	Me	1.37	1.5 °C[d]	-	0.29	-
14		H	Me	0.039	9.4 °C[d]	0.039f	0.37	4J21
15		H	Me	0.021	7.4 °C[d]	-	0.35	4J3M
16	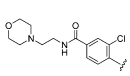	H	Me	0.022	9.9 °C[d]	0.018[f]	0.26	4J22
17	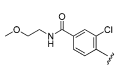	H	Me	0.009	10.1 °C[d]	0.016[f]	0.31	4J3L

[a]IC_{50} values are an average of two independent determinations. [b]Curves of the IC_{50} determination were impacted by the low solubility of the compounds. [c]Differential scanning fluorometry at 1000 μM. [d]Differential scanning fluorometry at 125 μM. [e]Surface plasmon resonance, steady-state analysis. [f]Surface plasmon resonance, kinetic analysis. [g]Ligand efficiency in pIC_{50}/HA, where HA means heavy atom, i.e., a non-hydrogen atom. [h]Several attempts to soak and cocrystallize the compounds were made, but no ligand density could be observed.

compound **11**, bearing an *o*-fluoro substituent (Table 1; compare to those with *p*-fluoro (compound **9**) and *m*-fluoro (compound **10**) substituents), invoking large T_m shifts even at lower ligand concentrations. We subsequently solved the structure of the protein−ligand complex of this compound, revealing that the newly added fluorophenyl moiety adopted a nonflat conformation (torsion of 51°, Figure 3) in which the fluorine atom had displaced a water molecule present in the structure of **2** (referred to as Wf below, Figures 2b and 4a). In addition, the aromatic group is lined up for van der Waals (vdW) interactions with the hydrophobic side chain of Ile1075 and nonpolar contact to Phe1035, Tyr1050, and Pro1034.

Affinity and Solubility Optimization. Further analysis of the crystal structures, and crystallographically directed molecular modeling of potential close analogues of **11**, suggested some additional features of the TNKS2 active site pocket that potentially could be exploited in the next iteration of compounds. When the fluorine atom in compound **11** displaces Wf, we conclude that this pocket could potentially harbor even larger *ortho*-substituents to maximize interactions with the carbonyl oxygen of Tyr1071 (Figure 4a). As mentioned above, **11** adopts a nonplanar conformation in the binding pocket. The conformational preferences of biphenyl torsions are sensitive to

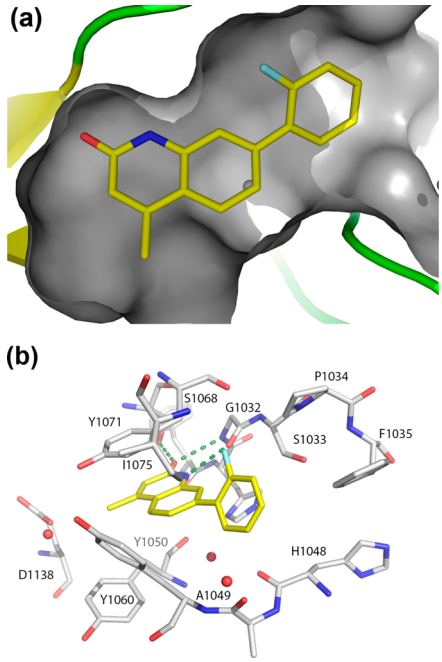

Figure 3. (a) Surface representation showing the overall positioning of compound **11** in the pocket. (b) Crystal structure of the active site of TNKS2 in complex with **11** showing the nonplanar binding conformation of the *o*-fluorophenyl moiety with hydrophobic interaction with Ile1075, Phe1035, and Tyr1050 as well as the *o*-fluoro interaction with the main chain oxygen of Tyr1071.

ortho-substituents. Altered conformational preference can, when it coincides with the binding conformation, have a dramatic influence on affinity,[15] which we decided to try to explore by introducing larger *ortho*-substituents. The crystal structure also suggests that *para*-substituents (Figure 3a) should be well accepted as this vector points toward the exit of the pocket and hence also a good area to sample polar features surrounding the exit and to introduce solubilizing groups if needed.

On the basis of this analysis, a set of 15 compounds was prepared (e.g., compounds **12** and **13**). The *o*-chloro compound **12** indeed led to larger T_m shifts than the *o*-fluoro analogue, and *para*-substituents were allowed as predicted, yielding substances with IC_{50} and K_d in the low nanomolar range. Interestingly, the activity of compound **13** is several orders of magnitude lower than that of **12**. Since no structural information is available for **13**, we cannot provide a structure-based understanding of why the difference in activity and stabilization of **13** and, for example, **8**, **11**, and **12** is so large. A possible explanation could be that **13** is unable to displace Wf and instead the additional bulkiness is only disruptive for the interaction. It was also apparent that some of the compounds containing *o*-chloro substituents behaved poorly and did not yield interpretable thermal shifts or crystal structures. We expected this, at least in part, to be due to solubility and or aggregation problems (Table 2). Hence, optimization of the *para*-position was done with these properties in mind, and some additional compounds (compounds **14**−**17**) were synthesized at this stage. Ligands synthesized extending on the *para*-position only allowed for limited interactions with the protein and mainly exposed these substituents to the solvent. In essence, these groups therefore served primarily as solubilizing groups, with concomitant loss of LE.

dx.doi.org/10.1021/jm400211f | J. Med. Chem. 2013, 56, 4497−4508

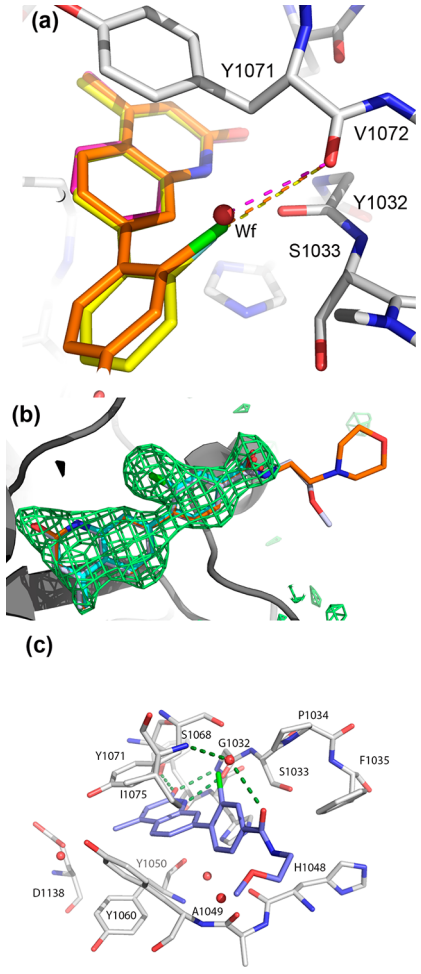

Figure 4. (a) Overlay of crystal structures of **2** (magenta), **11** (yellow), and **17** (orange) showing their interactions with the main chain carbonyl oxygen of Tyr1071. In the structure of the starting fragment **2**, Tyr1071 is hydrogen bonded to a water molecule, Wf (H_2O–O = 2.9 Å), that is displaced by F in **11** (F–O = 3.4 Å) and Cl in **17** (Cl–O = 3.0 Å). The Cl atom in the latter compound is distinctly closer to O(sp^2) than the average vdW radius (3.3 Å),[16] indicating an attractive electrostatic interaction between them. This is also supported by the near linear geometry of the C–Cl···O atoms. (b) Overlay of **16** (purple), **14** (cyan), and **17** (orange). The $F_o - F_c$ electrondensity map belongs to compound **17** (orange). (c) Crystal structure of **16** (purple) showing water-mediated interactions of the carbonyl oxygen and residue Ile1075 in addition to the hydrophobic interactions of the *o*-chlorophenyl with Tyr1071 and the hydrogen bonds to Ser1068 and Gly1032.

With this group the aggregation/solubility problems were resolved, as compounds with solubilizing functions in the *para*-position were immediately crystallographically productive (e.g., **14**–**17**) as well as behaved better in assays. Four crystal structures of protein–ligand complexes of the derivatives were subsequently solved. Upon analysis of these structures, we found that the Cl–O(Tyr1071) distance was 3.0 Å, distinctly shorter than the average Cl–O(sp^2) vdW radius of 3.3 Å, indicative of a electrostatic chlorine–carbonyl oxygen interaction (Figure 4a).[16] The *para*-substituents did vector out toward the exit of the pocket. For two compounds (**16** and **17**) bearing *p*-carboxamido substituents, the different N-attached alkyl tail clearly protrudes out of the pocket, making polar interactions with protein-anchored water molecules at the exit

Table 2. Solubility[a] of Selected Compounds

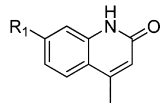

Cpd	R1	Solubility (μg/ml)
8	Ph	0.65
12		< 0.1
16	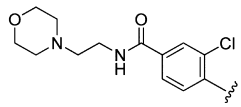	4.3
15	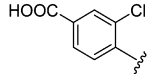	42.6

[a]Thermodynamic solubility (see the Experimental Section).

region to the main chain nitrogen of Ile1075 (Figure 4c). The solubilizing groups are clearly solvent immersed and very flexible, and it was not possible to model this part of the molecule into the electron density (Figure 4b).

Characterization of Ligands. All compounds were characterized using the DSF assay in a dose–response fashion (Figure 5a). In addition to the benefits mentioned before, this

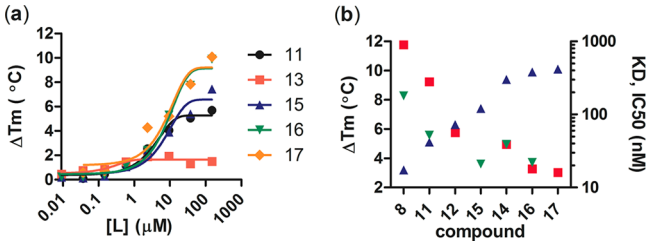

Figure 5. (a) DSF dose–response data on five compounds. (b) Comparison of the increase in thermal stability (DSF, blue) vs K_d (SPR, red) and IC_{50} (autoPARsylation, green) for a set of compounds prepared during the optimization. DSF was used for the library screen and as a primary metric during the optimization. The DSF assay was found to generally correlate well with IC_{50} and K_d (SPR).

also allowed us to seamlessly compare ligands at gradually lower concentrations as the affinity increased. As an example, fragments **2** and **3** show no significant stabilization at 125 μM, the concentration where the more high affinity ligands show clear effects.

A subset of the ligands discussed above was further characterized with SPR to follow the improvement of affinities along the compound evolution process. Good general correlations among SPR-derived K_d, IC_{50}, and responses from DSF were found (Table 1 and Figure 5b). For compounds for which SPR affinities were fitted by kinetic analysis, we examined the on- and off-rates. Overall, improvement in affinity generally follows the increasingly slower off-rates for the expanded compounds, although the situation becomes more complicated for the higher affinity compounds. For example, compounds **16** and **17** have essentially the same observed K_d with SPR (Table

dx.doi.org/10.1021/jm400211f | J. Med. Chem. 2013, 56, 4497–4508

1), but with quite different kinetic balances where the latter compound shows slower on- and off-rates. (SPR on- and off-rate data and plots are found in Figure S1 and Table S2, Supporting Information).

Selectivity. PARPs in general are key interference points in functional networks, a reason why they have spawned so much interest as targets for inhibitors. The most elaborate PARP inhibitors (such as **18** (olaparib)[17]) exhibit a relatively wide spectrum PARP inhibition profile. In contrast, our aim was to create potent inhibitors of TNKSs, if possible with no practical inhibition of other PARPs.

As compound **11** showed a significant jump in affinity, along with its novel binding mode, we decided to investigate the selectivity profile for this compound. We assayed **11** and **18** toward a panel of PARPs (Table 3) and found that **11** in contrast to **18** showed negligible inhibition at 10 μM.

Table 3. Inhibition (%) of Selected PARPs at 10 μM for Compounds 18 and 11

compd	PARP1	PARP2	PARP3	PARP6	PARP7	PARP11
11	21	2	0	31	37	23
18	97	99	99	98	84	72

We then generated more detailed data to compare with those of other inhibitors, particularly **1**. Interestingly, **11** is a very clean TNKS inhibitor, with more than 100-fold selectivity toward other PARPs (IC_{50} = 52 nM vs TNKS2). **1** is more potent than **11** but inhibits PARPs in the middle nanomolar range[6,18] (see Table 4 for a comparison). As shown in Table 1,

Table 4. IC_{50} (μM) and PARP Selectivity of 11 and 1[a]

compd	PARP1	PARP2	PARP3	TNK1	TNK2	PARP6
11	>10	>10	>10	0.86	0.052	>10
1	0.12	0.046	>10	0.011	0.008	>10

[a]PARP1, PARP2, PARP3, and PARP6 assays were performed by BPS Bioscience.

11 was later optimized further into compound **17**, which is a 5 times more potent inhibitor of TNKS2. The more potent compounds prepared in this study (**14**–**17**) all show a binding mode highly similar to that of **11**, and except for further exploiting the halo–O(sp^2) interactions with Tyr1071, they primarily introduce interactions in the exit region and solvent-immersed solubilizing functions. Because of these similarities, it is possible that the affinity gains (**14**–**17**) may be achievable with a maintained selectivity profile; however, this needs to be studied further, but it is clear that these compounds offer a new class of very PARP selective TNKS inhibitors.

Surprisingly, **11** also showed more than 16-fold selectivity for TNKS2 over TNKS1 (Table 4). Tankyrase inhibition has generally been studied as concurrent inhibition of both TNKS1 and TNKS2, and the knowledge of the specific contribution from the two enzymes is unclear. As there are no previous potent and intratankyrase-selective inhibitors, the pharmacological utility of compounds with these properties has not been explored. TNKS1 and TNKS2 often appear redundant[19] in knockout experiments, and data from Huang et al. indicate that simultaneous inhibition of TNKS1 and TNKS2 is required to increase the Axin levels.[6] The potential to use **11** and the more potent analogues as inhibitors of Wnt signaling therefore needs to be further investigated. On the other hand, this specificity profile enables therapies targeting TNKS2 without the potential side effects associated with inhibition of the Wnt pathway. These novel TNKS2-selective tool compounds can therefore provide an important chemical tool to study tankyrase biology.

Clearly, more studies on **11** and the more potent compounds developed in this study are needed to reveal the real potential for their use, but as mentioned above, as no intertankyrase-selective inhibitor has been available previously, pure inhibition effects are not well studied.

DISCUSSION

Several families of TNKS inhibitors have been described in the academic and patent literature;[8,9,20] however, so far none of these families have led to a clinical candidate. FBLD strategies identify hot spots in the protein for ligand binding and core fragments which are good starting points for ligand development.[21] The strategy can therefore generate more efficiently binding lead compounds as well as novel structural frameworks, as compared to existing compounds.

In this work, we have examined whether a fragment strategy is suitable for human TNKS and if it could be applied to discover novel compounds, with different properties as compared to existing TNKS inhibitors. The strategy used was initially driven by TSA screening, and each step was guided by X-ray structures of protein–ligand complexes. IC_{50} measurements were performed when higher affinity ligands were obtained, and SPR was used retrospectively to characterize improvements of affinities and ligand efficiency during fragment evolution. Albeit false negatives in initial TSA screens cannot be excluded, the strategy appeared efficient and led to the rapid development of high-affinity ligands for TNKS, with less than 40 compounds synthesized.

Most FBLD studies in the literature use NMR, SPR, or X-ray crystallography for initial fragment screening and evolution. We generally found the TSA-based data to be reliable for the TNKS2 system and to correlate well with other biophysical (SPR) and biochemical (autoPARsylation) data (Table 1 and Figure 5b).

As DSF, in contrast to NMR, requires protein and compounds at high concentration in the assay, it also, in effect, reports on compound issues that might hamper successful crystal soaking or cocrystallization of compounds. In practice, a major bottleneck of FBLD is the efficient translation of hits obtained from activity or biophysical assays into crystal structures. The protein concentration in crystals is very high (millimolar range), requiring high compound concentrations to achieve occupancy and interpretable densities of compounds in the crystal structures. Furthermore, the specific buffer and precipitant solutions in the soaking or cocrystallization experiment normally lower the effective compound solubility (Table 2). Therefore, hits can often be difficult to translate into structures of protein–ligand complexes. The indicative correlation for this was, for example, seen for compounds **12** and **8**, which appeared to reprecipitate in buffer preparations. In addition, they also showed low reproducibility in TSA assays and when soaked with TNKS2 crystals yielded crystal structures without bound ligand (data not shown). This problem was solved in the subsequent synthesis cycle where solubilities of the compounds were improved (Table 2).

As mentioned, we selected to optimize a scaffold based on compound **2**, although it has slightly lower ligand efficiency than **3**. The main reason was that **2** possesses better geometrical vectors for expansion in the pocket. In addition,

the binding mode of **2** was less overlapping with **1** and hence could provide more novel compounds.

It is interesting to note that compound **3**, a fragment not selected for expansion, is identical to the nicotinamide anchoring moiety of **18** (PDB 3U9Y),[12] and the binding conformation of this part of **18** and **3** can be completely superimposed (see the Supporting Information). **18** is primarily a PARP1−4 inhibitor (Table 4) and shows little interaction and stabilization with TNKS.[22] **18** is further extended using the vector occupied by a chlorine atom in **3**, an extension not structurally compatible (without perturbing the protein) in the crystal structure of **3**. As expected, the binding of **18** in TNKS2 invokes a conformational change in the D-loop, required to accommodate the rest of the compound. Although this shows that there is some degree of plasticity of the TNKS2 pocket, it also shows the risks of disturbing these residues, as this potentially is the reason for the lower affinity **18** shows toward TNKS2.

In contrast, the X-ray structures reveal that the orientation of the 2-hydroxy-4-methylquinoline scaffold is highly conserved and acts as an anchor all the way from compound **2**, the original fragment hit, to the more leadlike compounds **11** and **17** (Figure 6). This is in line with what other investigators have

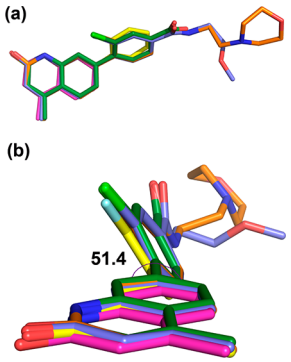

Figure 6. Overlay of the bound conformations extracted from protein−ligand crystal structures of the original fragment hit **2** (magenta), **11** (yellow), **15** (green), **16** (purple), and **17** (orange) showing that (a) the binding mode of the 2-hydroxyquinoline scaffold is conserved throughout the expansion of the fragment and (b) the biphenyl C−C−C−C torsion angles of the bound conformers are close to 51°.

reported for other fragment expansions previously[23] and lends support to the initial fragment **2** performing high-quality interactions. Also, the protein conformation is very conserved during fragment evolution, suggesting limited loss of binding energy due to protein conformational entropic costs upon binding.

The final compounds have several interesting properties that differentiate them from previous TNKS inhibitors. For example, substituents in *ortho*-positions can in addition to sampling direct interactions (Cl−carbonyl O(sp^2), water displacement in this case) also contribute significantly to affinity by altering the conformational preference of the compound by shifting the biaryl torsion from 30° to 40° for non-*ortho*-substituted derivatives vs 55° for *ortho*-substituted derivatives.[24] In effect, the ligands are preorganized in the binding conformation, and the observed biaryl torsion for the binding conformation in the crystal structures of all *ortho*-substituted compounds prepared is very close to 51° (Figure 6b). By reducing the conformational flexibility in solution, the entropic penalty upon binding to the protein is reduced. This is similar to a concept used in the design of protein tyrosine phosphatase-1B inhibitors[25] and inhibitors reviewed for other proteins.[15]

The compounds reported in this work are unique to previously reported TNKS and PARP inhibitors but have some similarities in binding mode. All earlier reported compounds, where TNKS structures are available for protein−ligand complexes, have their major interactions in the nicotinamide pocket, with the exception of 3-(4-methoxyphenyl)-5-({[5-methyl-4-(4-methylphenyl)-4*H*-1,2,4-triazol-3-yl]sulfanyl}methyl)-1,2,4-oxadiazole[8] (PDB 3UDD) and 4-(1,3,3a,4,7,7a-hexahydro-1,3-dioxo-4,7-methano-2*H*-isoindol-2-yl)-*N*-8-quinolinyl-benzamide[12] (IWR1, PDB 3UA9), which have major interactions in the adenine pocket with minor interactions in the nicotinamide pocket. One distinguishing feature of previous compounds binding in the nicotinamide-binding pocket is that they expanded further down into the pocket (toward Glu1138) as compared to the compounds of the present work, for example, **1** (Figure 7), but also 6(5*H*)-

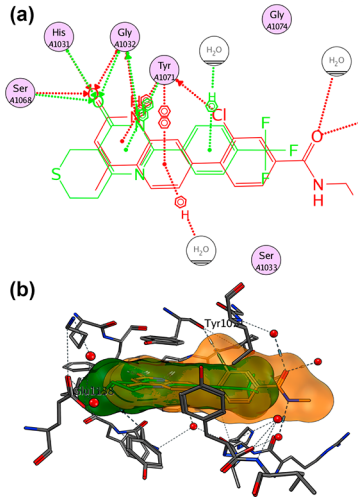

Figure 7. Comparison of the binding modes of **1** (PDB 3KR8) and **17** to TNKS2 based on crystal structures. Schematic (a) and molecular surface representation (b) overlay of the compounds interacting with the pocket. **1** is depicted in green and a representative of our series (**17**) in orange. To further illustrate the differences and similarities in binding modes, a molecular surface was created using the same colors.

phenanthridinone. This part of the pocket is highly conserved in both the TNKS and PARP families, and interactions in this pocket are a characteristic of several of the compounds with lower specificity between TNKS and PARP (primarily PARP1−4). The pocket contains the glutamate (Glu1138 in TNKS2) conserved in all family members that possess PARP activity, and our analysis suggests that none of the known compounds interacting in this pocket of TNKS (including our compound **2**) have managed to establish polar interactions with this carboxylate moiety.

Of the previously reported compounds, **1** stands out as a potential high-quality close-to-lead candidate, while other compounds suffer from either limited affinity or unsatisfactory LE. Although the compounds and binding modes in general are very different, the central interactions in the nicotinamide-binding pocket have similarities in **1** and our series; both make

dx.doi.org/10.1021/jm400211f | *J. Med. Chem.* 2013, 56, 4497−4508

a π-bonded interaction with a protein-bound water (Figure 7). In our series this is by the second ring of the quinolinone moiety, while for **1** it is accomplished by the (trifluoromethyl)-aryl ring. As discussed above, the cyclic thioether moiety of **1** makes interactions in the Glu1138 pocket including the residue Phe1061 (3.58 Å), while this space is occupied by a water molecule in, for example, the structure with compound **15** (CH_3–H_2O = 3.1 Å, H_2O–Glu1138 = 3.1 Å, H_2O–Phe1061 = 2.8 Å). Although **1** fits nicely in this pocket, it does not make polar interactions with Glu1138. The most striking differences are seen at the other end of the compound, where in our series a chlorine atom explores a novel interaction with Tyr1071, substituting a water molecule present in other inhibitor structures. This is enabled by the nonplanar geometry (torsion is near 51°) between the hydroxyquinoline moiety and the *o*-halo-substituted ring seen in all our structures.

Superposition of TNKS2 in complex with compound **11** onto PARP2 (PDB 3KJD) reveals that the amino acids responsible for the interactions around the 2-hydroxy-4-methylquinoline part of the compound are well conserved. However, a patch of much less conserved hydrophobic residues is apparent in the *o*-chloro-binding site: Pro1034, Phe1035, and the aromatic ring of Tyr1050 in the D-loop (Figure 8). The D-loop in TNKS is shorter than in PARP1–4.[20,22] In addition, in the structure of TNKS2, the loop containing Ile1075 closes down much more onto the substrate-binding site than the equivalent amino acids in PARP2.

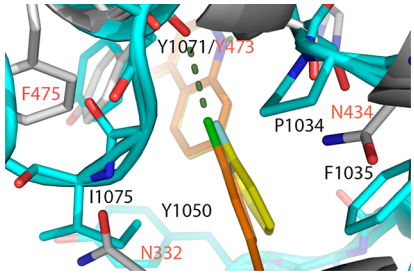

Figure 8. Binding of compound **11** (yellow) and compound **17** (orange) to TNKS2 (blue) compared to PARP2 (gray) showing the differences/similarities in substrate-binding area between the proteins. The amino acids in TNKS2 are marked in gray and those in PARP2 in orange.

There are also some hydrophilic residues from the α-helix-5 from the regulatory domain in the PARP2 structure near the NAD+ cleft opening (this domain is not present in TNKS2). In the superposition of the proteins, these hydrophilic amino acids reach into the binding site and clash with the compounds in the TNKS2 structures.

Overall, this region of the binding cavity in TNKS2 contains more hydrophobic residues than in PARP2 and other members of the PARP family.[20,22] This could also describe the selectivity of compound **11** as an explicit TNKS inhibitor.

CONCLUSION

In conclusion, a new class of potent TNKS inhibitors has been developed using a TSA-driven fragment-based approach where major expansions were guided by crystal structures and the activity improvments were monitored throughout the process. Key compounds were further characterized using SPR to establish that TSA and IC_{50} values correlated with an improvement of K_d. Chemical expansion was started from nicotinamide-pocket-anchored fragments which were grown to exploit a novel chloro–O(sp^2) interaction with the main chain carbonyl oxygen of Tyr1071. In the final rounds of chemistry, additional efforts were made to improve the physicochemical properties of the compounds in the series and a set of solubility-improving modifications were introduced to generate compounds that have high affinity, good physicochemical properties, and a unique selectivity profile.

EXPERIMENTAL SECTION

Protein Expression and Purification. The TNKS2 PARP domain (amino acids 947–1162) was produced in *Escherichia coli* and purified using Ni chromatography as previously described.[18] This protein construct was used for biophysical characterization (DSF and SPR) and X-ray crystallography.

Fragment Screening and Biophysics. *Compound Library.* A 500 compound fragment library was acquired from Maybridge (RO3 500 library 2009 Maybridge (Trevillett, Tintagel, Cornwall, U.K.)).

Differental Scanning Flourometry. A DSF assay was used to probe compound effects on TNKS2 thermal stability. The protein was diluted to 0.2 mg/mL in buffer containing (1:1000, 5×) SYPRO Orange (Invitrogen). We added 0.5 μL of either compound solution or DMSO control, making the final volume 25 μL in all wells. Melt analysis was performed on an ICycler IQ (Bio-Rad) real-time PCR instrument with filters set up for detection of SYPRO Orange ($\lambda_{excitation}$ = 490 nm, $\lambda_{emission}$ = 575 nm) fluorescence. The plates were covered in optically clear tape before initiation of the experiment, where a temperature interval of 25–80 °C was scanned at a ramp rate of approximately 2 °C/min.

For fragment screening, the compounds were added from stocks in 50 mM DMSO, giving an end compound concentration of 1 mM and a DMSO concentration of 2%. The compounds were plated in a layout of 80 fragments and 16 DMSO controls for each 96-well plate. Analysis of the screen data was primarily done by ocular inspection of individual curves, and fitting T_m to sigmoidal transitions where applicable was performed using an Excel script.[26] For dose–response data and DSF assay on expansion compounds made at various concentrations, dilution of the compounds was done in 100% DMSO at 50× assay concentration. For data generated with in situ digestion of TNKS2, trypsin, 1:100 (m/m) vs TNKS2, was added to the protein buffer dye mixture just prior to the DSF experiment.

DSF in Situ Digestion of TNKS2. To try to simplify the interpretation of the thermal shift data, we decided to investigate the use of in situ trypsination in combination with DSF. In situ trypsination is commonly used in crystallography as a way to promote crystallization,[27] presumably by removing less ordered and well-folded contaminants. It has previously been described to work well on TNKS2 for crystallization purposes.[18] Chymotrypsin (1/100 TNKS2 mass equivalents) was added to the protein buffer dye mixture just prior to the DSF experiment. This provided much cleaner curves, which substantially simplified the interpretation and fitting of the weakly shifting original fragment hits.

Surface Plasmon Resonance. All measurements were performed using a Biacore T200 (GE Healthcare) using a running buffer of 20 mM PBS, pH 7.4, 0.05% Tween20, and 2% DMSO. TNK2 was immobilized using a capture-coupling protocol very similarly to what has previously been described.[28] Briefly, TNK2–6HIS (20 μg/mL) in 20 mM PBS buffer, pH 7.4, was introduced with a flow rate of 10 μL/min to a Ni^{2+} and NHS doubly preactivated NTA chip (NTA-S Biacore BR-1005-32) with a response target of 5000 RU. This procedure led to a stable and robust surface of about 4600 RU, which was used for further characterization.

For the kinetic experiments, the T200 standard method LMW kinetic was used with a contact time 60 s and a dissociation time of 3000 s at a flow rate of 30 μL/min. For more details on sample preparation and the experimental layout, see the Supporting Information. Analysis of the SPR data was performed using Biacore T200 evaluation software and Scrubber2.[29]

Crystallography. TNKS2 crystals were obtained from chymotrypsin-cleaved TNK at a concentration of 10.5 mg/mL in hanging drops at 4 °C in 0.1 M Tris−HCl, pH 8.5, 15−20% PEG3350, and 0.2 M lithium sulfate as previously described.[18] The crystals were then transferred to a solution containing a 0.5 mM (5% DMSO) concentration of the ligand of interest and soaked for about 2 h up to overnight before they were flash frozen in liquid nitrogen. Glycerol (20%) was used as a cryoprotectant.

Diffraction data for the complexes were collected to resolutions between 1.9 and 2.4 Å on the BL13B1 beamline (ADSC Quantum-315 CCD detector) at the National Synchrotron Radiation Research Center (NSRRC), Taiwan, ROC, as well as on the MX1 beamline at the Australian Synchrotron, Victoria, Australia.

The crystals belonged to space group $C222_1$ (unit cell parameters a = 94 Å, b = 94 Å, and c = 116 Å) with 2 molecules/ASU or $P2_12_12_1$ (unit cell parameters a = 67 Å, b = 67 Å, and c = 118 Å) with 4 molecules/ASU.

At the Australian synchrotron, Blu-Ice[30] was used for data collection and processing. All the other data were processed using HKL2000[31] and mosflm,[32] and the structures were solved with molecular replacement using Phaser[33] from the CCP4 program suite, with the apo structure (PDB 3KR7) as a model.[34] Model building was done using COOT[35] and refinement using Refmac.[36] The ligand CIF libraries were generated using Corina,[37] and the ligand, Zn ion, and some sulfate ions were fitted into the electron density using COOT and refined further.

Details on data processing and refinement statistics are given in the Supporting Information, Table S2.

Pymol[38] and MOE2011.10[39] were used for constructing the structure figures.

Chemistry. *General Procedures.* All reagents were purchased from commercial sources and used as received. Reaction progress was monitored by TLC using Merck silica gel 60 F254 on glass plates with detection by UV at 254 nM. LC−MS analysis was carried out with a Shimadzu LC-20AD and LCMS-2020. The column used was a Phenomenex Kinetex 2.6 μm, 50 × 2.10 mm). Proton nuclear magnetic resonance (^{1}H NMR) spectra were obtained using a Bruker Ultrashield 400 PLUS/R system, operating at 400 MHz. All resonance bands were referenced to tetramethylsilane (internal standard). Splitting patterns are indicated as follows: s, singlet; d, doublet; t, triplet; m, multiplet; br, broad peak. The compounds' purities were ≥95% determined by a VARIAN ProStar HPLC instrument. Melting points were determined in Pyrex capillary tubes using a StuartnSMP30 melting point apparatus.

Thermodynamic Solubility Study. A 6 μL volume of 50 mM DMSO stock from the stock plate is added to the reaction deep well plate containing 600 μL of pH 4.0 pION buffer, mixed, and incubated for 18 h. The plate is sealed well during the incubation process. The test compound concentration is 500 μM. At the end of the incubation period, 100 μL of sample from the storage plate is vacuum filtered using a filter plate. This step wets the filters, and the filtrate is discarded. Another 200 μL of the sample from the deep well plate is vacuum filtered using the same filter block but a clean filter plate. A 75 μL volume of the filtrate from the filter plate is transferred to a UV sample plate. A 75 μL volume of 1-propanol is added to this UV plate. The solution is mixed, and the spectrum is read using the UV spectrophotometer (Spectramax-Molecular Devices). The analysis is carried out by using pION μSOL EXPLORER software, version 3.3.

*Synthesis. N-(3-Bromophenyl)-3-oxobutanamide (**4**).* A solution of ethyl acetoacetate (10 g, 58.1 mmol) in dry toluene (58 mL) was added to 3-bromoaniline (12.1 g, 93 mmol) in a dropwise manner in a round-bottomed flask, and the reaction mixture was refluxed overnight. Upon completion of reaction, the reaction mixture was cooled and quenched with sodium carbonate solution. The aqueous fraction was extracted with dichloromethane; the organics were dried over sodium sulfate and concentrated in vacuo to give a brown residue. Hexane was added to the residue, and the flask was cooled with ice to aid precipitation of the product. A light brown precipitate of **4** (6.3 g, yield 42%) was obtained after filtration via a Buchner funnel: ^{1}H NMR (400 MHz, DMSO-d_6) δ (ppm) 10.26 (br s, 1 H), 7.96 (s, 1 H), 7.46 (d, J = 7.60 Hz, 1 H), 7.32−7.23 (m, 2 H), 3.58 (s, 2 H), 2.19 (s, 3 H); MS (ESI) m/z $[C_{10}H_{10}BrNO_2 + H]^+$ 257.

*7-Bromo-4-methyl-1,2-dihydroquinolin-2-one (**5**).* A mixture of **4** (6.3 g, 24.6 mmol) and concentrated sulfuric acid (30 mL) was heated to 120 °C and stirred for 2 h. Upon completion of reaction, the reaction mixture was cooled and poured into ice. The resulting precipitate was filtered and washed with water and ether. The crude material was then recrystallized from methanol to give **5** as a colorless solid (4 g, yield 68%): ^{1}H NMR (400 MHz, DMSO-d_6) δ (ppm) 11.65 (br s, 1 H), 7.65 (d, J = 8.53 Hz, 1 H), 7.48 (d, J = 2.01 Hz, 1 H), 7.35 (dd, J = 8.53, 1.88 Hz, 1 H), 6.43 (s, 1 H), 2.40 (d, J = 0.88 Hz, 3 H); MS (ESI) m/z $[C_{10}H_8BrNO + H]^+$ 239.

*General Synthetic Route for Compounds **7**−**15**.* A solution of **5** (0.21 mmol) in 4:1 dioxane/water (2.1 mL) was added to the corresponding boronic acid (0.42 mmol). Potassium carbonate (0.53 mmol) was added to the reaction mixture, followed by tetrakis-(triphenylphosphine)palladium (0.02 mmol). The reaction mixture was heated to reflux and allowed to stir overnight. Upon completion, the reaction mixture was cooled to room temperature, and the solvent was removed by rotary evaporation. The residue was poured into water and extracted with dichloromethane. The organic layer was dried over sodium sulfate and filtered, and the solvent was removed by rotary evaporation. The crude material was then recrystallized from ethyl acetate/dichloromethane/hexane to give a colorless solid.

*4-Methyl-6-phenyl-1,2-dihydroquinolin-2-one (**7**).* **7** was prepared according to the general procedure using commercially available 6-bromo-4-methyl-1,2-dihydroquinolin-2-one and 4,4,5,5-tetramethyl-2-phenyl-1,3,2-dioxaborolane as reactants. The crude material was recrystallized from ethyl acetate/dichloromethane/hexane to give **7** as a colorless solid (yield 81%, mp 266−268 °C): ^{1}H NMR (400 MHz, chloroform-d) δ (ppm) 11.45 (br s, 1 H), 7.86 (d, J = 1.60 Hz, 1 H), 7.76 (d, J = 1.60 Hz, 1 H), 7.74 (d, J = 1.6 Hz, 2 H), 7.68−7.46 (m, 3 H), 7.43 (d, J = 8.4 Hz, 1 H), 7.0 (s, 1 H), 2.52 (s, 3 H); MS (ESI) m/z $[C_{16}H_{13}NO + H]^+$ 236.

*4-Methyl-7-phenyl-1,2-dihydroquinolin-2-one (**8**).* **8** was prepared according to the general procedure using **5** and commercially available 4,4,5,5-tetramethyl-2-phenyl-1,3,2-dioxaborolane as reactants. The crude material was recrystallized from ethyl acetate/dichloromethane/hexane to give **8** as a colorless solid (yield 47%, mp 290−292 °C): ^{1}H NMR (400 MHz, chloroform-d) δ (ppm) 10.38 (br s, 1 H), 7.74 (d, J = 8.4 Hz, 1 H), 7.65 (d, J = 7.60 Hz, 2 H), 7.55−7.43 (m, 5 H), 6.56 (s, 1 H), 2.52 (s, 3 H); MS (ESI) m/z $[C_{16}H_{13}NO + H]^+$ 236.

*7-(4-Fluorophenyl)-4-methyl-1,2-dihydroquinolin-2-one (**9**).* **9** was prepared according to the general procedure using **5** and commercially available 2-(4-fluorophenyl)-4,4,5,5-tetramethyl-1,3,2-dioxaborolane as reactants. The crude material was recrystallized from dichloromethane/methanol/hexane to give **9** as a colorless solid (yield 34%, mp 255−257 °C): ^{1}H NMR (400 MHz, chloroform-d) δ (ppm) 10.51 (br s, 1 H), 7.73 (d, J = 8.0 Hz, 1 H), 7.63 (dd, J = 3.2, 6.4 Hz, 2 H), 7.48 (d, J = 8.4 Hz, 1 H), 7.44 (s, 1H), 7.18 (m, 2 H), 6.57 (s, 1 H), 2.53 (s, 3 H); MS (ESI) m/z $[C_{16}H_{12}FNO + H]^+$ 254.

*7-(3-Fluorophenyl)-4-methyl-1,2-dihydroquinolin-2-one (**10**).* **10** was prepared according to the general procedure using **5** and commercially available (3-fluorophenyl)boronic acid as reactants. The crude material was recrystallized from dichloromethane/methanol/hexane to give **10** as a colorless solid (yield 20%, mp 264−266 °C): ^{1}H NMR (400 MHz, chloroform-d) δ (ppm) 10.51 (br s, 1 H), 7.75 (d, J = 8.4 Hz, 1 H), 7.48−7.27 (m, 5 H), 7.13−7.09 (m, 1 H), 6.58 (s, 1 H), 2.53 (s, 3 H); MS (ESI) m/z $[C_{16}H_{12}FNO + H]^+$ 254.

*7-(2-Fluorophenyl)-4-methyl-1,2-dihydroquinolin-2-one (**11**).* **11** was prepared according to the general procedure using **5** and commercially available (2-fluorophenyl)boronic acid as reactants. The crude material was recrystallized from dichloromethane/methanol/hexane to give **11** as a colorless solid (yield 20%, mp 285−287 °C): ^{1}H NMR (400 MHz, chloroform-d) δ (ppm) 9.77 (br s, 1 H), 7.74 (d, J = 8.4 Hz, 1 H), 7.50−7.39 (m, 4 H), 7.27−7.17 (m, 2 H), 6.57 (s, 1 H), 2.52 (s, 3 H); MS (ESI) m/z $[C_{16}H_{12}FNO + H]^+$ 254.

*7-(2-Chlorophenyl)-4-methyl-1,2-dihydroquinolin-2-one (**12**).* **12** was prepared according to the general procedure using **5** and

commercially available (2-chlorophenyl)boronic acid as reactants. The crude material was recrystallized from dichloromethane/methanol/hexane to give **12** as a colorless solid (yield 49%, mp 275−277 °C): ^{1}H NMR (400 MHz, chloroform-*d*) δ (ppm) 10.10 (br s, 1H), 7.73 (d, J = 8.28 Hz, 1 H), 7.48−7.54 (m, 1 H), 7.31−7.40 (m, 4 H), 7.29 (s, 1 H), 6.58 (s, 1 H), 2.54 (s, 3 H); MS (ESI) m/z $[C_{16}H_{12}ClNO + H]^+$ 270.

*7-(2-Methoxyphenyl)-4-methyl-1,2-dihydroquinolin-2-one (**13**).* **13** was prepared according to the general procedure using **5** and commercially available (2-methylphenyl)boronic acid as reactants. The crude material was recrystallized from dichloromethane/methanol/hexane to give **13** as a colorless solid (yield 27%, mp 270−273 °C): ^{1}H NMR (400 MHz, chloroform-*d*) δ (ppm) 11.50 (br s, 1H), 7.71 (d, J = 8.4 Hz, 1 H), 7.42−7.32 (m, 4 H), 7.09−7.00 (m, 2 H), 6.53 (s, 1 H), 3.84 (s, 3 H), 2.51 (s, 3 H); MS (ESI) m/z $[C_{17}H_{15}NO_2 + H]^+$ 266.

*7-(4-Amino-2-chlorophenyl)-4-methylquinolin-2(1H)-one (**14**).* **14** was prepared according to the general procedure using commercially available 6-bromo-4-methyl-1,2-dihydroquinolin-2-one and 3-chloro-4-(4,4,5,5-tetramethyl-1,3,2-dioxaborolan-2-yl)aniline as reactants. The crude material was recrystallized from ethyl acetate/dichloromethane/hexane to give **14** as a colorless solid (yield 33%, mp 264−266 °C): ^{1}H NMR (400 MHz, chloroform-*d*) δ (ppm) 9.71 (br s, 1 H), 7.69 (d, J = 8.4 Hz, 1 H), 7.76 (dd, J = 8.4 Hz, 1.60 Hz, 1 H), 7.31 (d, J = 1.6 Hz, 2 H), 7.22 (s, 1 H), 7.16 (d, J = 8.4 Hz, 1 H), 6.81 (s, J = 2.4 Hz, 1 H), 6.65 (dd, J = 8 Hz, 2.4 Hz, 1 H), 6.54 (s, 1 H), 2.51 (s, 3 H); MS (ESI) m/z $[C_{16}H_{13}NO + H]^+$ 285.

*3-Chloro-4-(4-methyl-2-oxo-1,2-dihydroquinolin-7-yl)benzoic Acid (**15**).* **15** was prepared according to the general procedure using **5** and commercially available 3-chloro-5-(tetramethyl-1,3,2-dioxaborolan-2-yl)benzoic acid as reactants. Upon completion, the reaction was filtered through Celite and washed with methanol. The filtrate was acidified to pH 2, extracted with isopropyl alcohol/dichloromethane (1:7), dried over magnesium sulfate, and evaporated to dryness in vacuo. The crude material was recrystallized from dichloromethane/methanol/hexane. **15** was obtained as a colorless solid (yield 33%, mp > 370 °C): ^{1}H NMR (400 MHz, D_2O) δ (ppm) 11.68 (s, 1H), 8.02 (s, 1 H), 7.94 (d, J = 7.6 Hz, 1 H), 7.81(d, J = 8 Hz, 1 H), 7.51 (d, J = 7.6 Hz, 1 H), 7.38 (d, J = 1.6 Hz), 7.26 (d, J = 7.6 Hz, 1H), 6.45 (s, 1 H), 2.47 (s, 3 H); MS (ESI) m/z $[C_{17}H_{12}ClNO_3 + H]^+$ 314.

*General Synthesis Route for Compounds **16** and **17**.* A solution of **15** (0.064 mmol) in *N*,*N*-dimethylformamide (1 mL) was added to *N*,*N*-diisopropylethylamine (0.03 mL) and 2-(1*H*-7-azabenzotriazol-1-yl)-1,1,3,3-tetramethyluronium hexafluorophosphate methanaminium (0.14 mmol) and the resulting solution stirred for 10 min before addition of the corresponding amine (0.127 mmol). The solution was left to stir at room temperature for 2 h. Upon completion, the reaction was extracted with dichloromethane, dried over magnesium sulfate, and evaporated to dryness in vacuo. The crude material was purified by recrystallization with methanol to afford a white solid.

*3-Chloro-4-(4-methyl-2-oxo-1,2-dihydroquinolin-7-yl)-N-[2-(morpholin-4-yl)ethyl]benzamide (**16**).* **16** was prepared according to the general procedure using **15** and commercially available 4-(2-aminoethyl)morpholine as reactants. The crude material was purified by recrystallization with methanol to afford **16** as a white solid (yield 12%, mp 165−169 °C): ^{1}H NMR (400 MHz, DMSO-d_6) δ (ppm) 11.68 (s, 1 H), 8.62 (t, J = 5.3 Hz, 1 H), 8.04 (d, J = 1.5 Hz, 1 H), 7.90 (d, J = 8.1 Hz, 1H), 7.81 (d, J = 8.4 Hz, 1 H), 7.56 (d, J = 8.0 Hz, 1 H), 7.36 (s, 1 H), 2.43 (m, 4 H), 7.27 (dd, J = 1.6, 8.0 Hz, 1 H), 6.46 (s, 1 H), 3.58 (m, 5 H), 3.42 (m, 3 H), 2.47 (s, 3 H); MS (ESI) m/z $[C_{23}H_{24}ClN_3O_3 + H]^+$ 426.

*3-Chloro-N-(2-methoxyethyl)-4-(4-methyl-2-oxo-1,2-dihydroquinolin-7-yl)benzamide (**17**).* **17** was prepared according to the general procedure using **15** and commercially available 2-methoxyethylamine as reactants. The crude material was purified by recrystallization with methanol to afford **17** as a white solid (yield 21%, mp 257−158 °C): ^{1}H NMR (400 MHz, DMSO-d_6) δ (ppm) 11.68 (s, 1 H), 8.74 (t, J = 5.1 Hz, 1 H), 8.06 (d, J = 1.6 Hz, 1 H), 7.93 (dd, J = 1.6, 8.0 Hz, 1 H), 7.81 (d, J = 8.2 Hz, 1 H), 7.55 (d, J = 8.0 Hz, 1 H), 7.37 (d, J = 1.4 Hz, 1 H), 7.27 (dd, J = 1.6, 8.3 Hz, 1 H), 6.46 (s, 1 H), 3.47−3.48 (m, 4 H), 3.28 (s, 3 H), 2.46 (s, 3 H); MS (ESI) m/z $[C_{20}H_{19}ClN_2O_3 + H]^+$ 371.

Biological Assays. *TNKS2 DNA Cloning and Protein Production.* The gene encoding the PARP domain of TNKS2 (amino acids 934−1166) was synthesized (GenScript, Piscataway, NJ) with *Eco*RI and *Sal*I sites at the 5′ and 3′ ends of the gene to allow in-frame subcloning into the expression vector pGEX-6P-1.

Gene expression in BL21(DE3) cells (Merck, Germany) was performed in the presence of 0.5 mM IPTG at 18 °C for 18 h. The recombinant protein was purified by immobilized affinity chromatography (IMAC) on the Profinia protein purification system (Bio-Rad, Hercules, CA). The protein was eluted in elution buffer containing 20 mM glutathione. The purified protein was concentrated using a 10 mL concentrator with cellulose membrane, 10 kDa NMWL. By successive 30 min centrifugation, the glutathione buffer was exchanged for 0.1 M Tris buffer, pH 8.0. The protein was concentrated to about 1.1 mg/mL. The amount of purified protein obtained from a 1 L induction was 8.9 mg. The resultant protein has a purity of ∼91% as determined by the 2100 bioanalyzer (Agilent, Santa Clara, CA).

The auto-PARsylation reactions were carried out in 40 μL volumes in the presence of the compound (concentration varying from 0.006 to 100 μM, 2.5% DMSO), 20 nM GST-TNKS2, and 250 μM NAD+ (Sigma-Aldrich). The reactions were incubated at room temperature for 2 h and then quenched by adding 10 μL of 20% formic acid. Then 100 μL of acetonitrile was added, and the samples were centrifuged for 30 min at 3500 rpm and 4 °C. The supernatant was transferred to a new plate and subjected to the LC/MS analysis.

Analytical Method. HPLC−MS/MS analysis was carried out using an Agilent 1200RRLC series HPLC system consisting of a binary pump, vacuum degasser, and column switching valve with an autosampler equipped with a 40 μL sample loop interfaced with a TSQ quantum ultra triple-stage quadrupole tandem mass spectrometer (Thermo Scientific). Both systems were controlled by either XCalibur or LCQuan software. Nicotinamide was separated onto a Phenomenex Kinetex—HILIC column (50 × 2.1 mm, 2.6 μM) using mobile phases (mobile phase A, 0.1% formic acid in Milli-Q water with 10 mM ammonium formate; mobile phase B, 0.1% formic acid in acetonitrile). The isocratic LC method was run at 0.4 mL/min with 70% mobile phase B with a run time of 2 min.

The mass spectrometer was operated with positive ion detection for nicotinamide. The selected reaction monitoring (SRM) transition for nicotinamide was m/z 123 → 79.7. The vaporization temperature was maintained at 400 °C, and a voltage of 4 kV was applied to the sprayer needle. Nitrogen gas was used as the sheath gas and auxiliary gas. The argon gas was used for the collision energy. The detection and relative quantification of analytes were performed using the SRM mode.

Data Processing/Analysis. The chromatogram data were acquired by LCQuan software. The raw data from each sample were processed by a processing method for each batch of sequences. The quantification of an individual component as a peak area was done in arbitrary units. The area of the peak corresponding to nicotinamide on the MS chromatogram was plotted against the log of compound concentrations. The experimental data were analyzed by nonlinear regression (GraphPad Prism).

Computational Tools. Instant JChem 5.9.0 was used for structure database management, search, and prediction (ChemAxon, 2012, http://www.chemaxon.com).

The protein−ligand crystal structures of both initial fragment hits and the expansions were analyzed and visualized using Lead-IT v2.1 (2012, www.Biosolveit.com/LeadIT) and MOE (Molecular Operating Environment), version 2011.10 (Chemical Computing Group, Montreal, Canada, http://www.chemcomp.com/software.htm).

■ ASSOCIATED CONTENT

Ⓢ Supporting Information

Table with SPR data for on- and off-rates, table of crystallographic details for all X-ray structures, figure showing the superpositioning of compounds **3** and **18** binding to TNKS2, list of less successful modifications of **2** and related

compounds, dose−response data on fragment hits **2** and **3**, and table on methods used for PARP1 activity assays. This material is available free of charge via the Internet at http://pubs.acs.org.

Accession Codes

The crystal structures of compounds **2**, **3**, **11**, **14**, **15**, **16**, and **17** in complex with TNKS2 have been deposited with the RCSB Protein Data Bank under the accession codes 4JIZ, 3W5I, 41UE, 4J21, 4J22, 4J3L, 4J3M.

AUTHOR INFORMATION

Corresponding Author

*E-mail: andreas.larsson@ntu.edu.sg, +65 65869756 (E.A.L.);pnordlund@ntu.edu.sg, +65 65869693(P.N.).

Author Contributions

[‖]E.A.L. and A.J. contributed equally to this work.

Notes

The authors declare no competing financial interest.

ACKNOWLEDGMENTS

Portions of this research were carried out at the National Synchrotron Radiation Research Center, a national user facility supported by the National Science Council of Taiwan, Republic of China. The Synchrotron Radiation Protein Crystallography Facility is supported by the National Research Program for Genomic Medicine. This research was also undertaken on the MX1 beamline at the Australian Synchrotron, Victoria, Australia. We thank the beamline staff at both the synchrotrons for all their help during data collection. This work was supported by funding from a principal investigator start-up grant from Nanyang Technological University, the National Research Foundation (Grant NRF-CRP4-2008-02), and the Biomedical Research Council.

ABBREVATIONS USED

FBLD, fragment-based ligand design; SPR, surface plasmon resonance; DSF, differential scanning fluorometry; NAD+, nicotinamide adenine dinucleotide; PARP, poly(ADP-ribose) polymerase; TNKS, tankyrase (TRF1-interacting, ankyrin-related ADP-ribose polymerase)

REFERENCES

(1) Fancy, S. P. J.; Harrington, E. P.; Yuen, T. J.; Silbereis, J. C.; Zhao, C.; Baranzini, S. E.; Bruce, C. C.; Otero, J. J.; Huang, E. J.; Nusse, R.; Franklin, R. J. M.; Rowitch, D. H. Axin2 as regulatory and therapeutic target in newborn brain injury and remyelination. *Nat. Neurosci.* **2011**, *14*, 1009−1016.

(2) D'Amours, D.; Desnoyers, S.; D'Silva, I.; Poirier, G. G. Poly(ADP-ribosyl)ation reactions in the regulation of nuclear functions. *Biochem. J.* **1999**, *342* (Part2), 249−268.

(3) Smith, S.; Giriat, I.; Schmitt, A.; de Lange, T. Tankyrase, a poly(ADP-ribose) polymerase at human telomeres. *Science* **1998**, *282*, 1484−1487.

(4) Rouleau, M.; Patel, A.; Hendzel, M. J.; Kaufmann, S. H.; Poirier, G. G. PARP inhibition: PARP1 and beyond. *Nat. Rev. Cancer* **2010**, *10*, 293−301.

(5) Riffell, J. L.; Lord, C. J.; Ashworth, A. Tankyrase-targeted therapeutics: expanding opportunities in the PARP family. *Nat. Rev. Drug Discovery* **2012**, *11*, 923−936.

(6) Huang, S.-M. A.; Mishina, Y. M.; Liu, S.; Cheung, A.; Stegmeier, F.; Michaud, G. A.; Charlat, O.; Wiellette, E.; Zhang, Y.; Wiessner, S.; Hild, M.; Shi, X.; Wilson, C. J.; Mickanin, C.; Myer, V.; Fazal, A.; Tomlinson, R.; Serluca, F.; Shao, W.; Cheng, H.; Shultz, M.; Rau, C.; Schirle, M.; Schlegl, J.; Ghidelli, S.; Fawell, S.; Lu, C.; Curtis, D.; Kirschner, M. W.; Lengauer, C.; Finan, P. M.; Tallarico, J. A.; Bouwmeester, T.; Porter, J. A.; Bauer, A.; Cong, F. Tankyrase inhibition stabilizes axin and antagonizes Wnt signalling. *Nature* **2009**, *461*, 614−620.

(7) Waaler, J.; Machon, O.; Tumova, L.; Dinh, H.; Korinek, V.; Wilson, S. R.; Paulsen, J. E.; Pedersen, N. M.; Eide, T. J.; Machonova, O.; Gradl, D.; Voronkov, A.; von Kries, J. P.; Krauss, S. A novel tankyrase inhibitor decreases canonical Wnt signaling in colon carcinoma cells and reduces tumor growth in conditional APC mutant mice. *Cancer Res.* **2012**, *72*, 2822−2832.

(8) Shultz, M. D.; Kirby, C. A.; Stams, T.; Chin, D. N.; Blank, J.; Charlat, O.; Cheng, H.; Cheung, A.; Cong, F.; Feng, Y.; Fortin, P. D.; Hood, T.; Tyagi, V.; Xu, M.; Zhang, B.; Shao, W. [1,2,4]Triazol-3-ylsulfanylmethyl)-3-phenyl-[1,2,4]oxadiazoles: antagonists of the Wnt pathway that inhibit tankyrases 1 and 2 via novel adenosine pocket binding. *J. Med. Chem.* **2012**, *55*, 1127−1136.

(9) Chen, B.; Dodge, M. E.; Tang, W.; Lu, J.; Ma, Z.; Fan, C.-W.; Wei, S.; Hao, W.; Kilgore, J.; Williams, N. S.; Roth, M. G.; Amatruda, J. F.; Chen, C.; Lum, L. Small molecule-mediated disruption of Wnt-dependent signaling in tissue regeneration and cancer. *Nat. Chem. Biol.* **2009**, *5*, 100−107.

(10) Peterson, R. T. Drug discovery: propping up a destructive regime. *Nature* **2009**, *461*, 599−600.

(11) Ferraris, D. V. Evolution of poly(ADP-ribose) polymerase-1 (PARP-1) inhibitors. From concept to clinic. *J. Med. Chem.* **2010**, *53*, 4561−4584.

(12) Narwal, M.; Venkannagari, H.; Lehtiö, L. Structural basis of selective inhibition of human tankyrases. *J. Med. Chem.* **2012**, *55*, 1360−1367.

(13) Niesen, F. H.; Berglund, H.; Vedadi, M. The use of differential scanning fluorimetry to detect ligand interactions that promote protein stability. *Nat. Protoc.* **2007**, *2*, 2212−2221.

(14) Abad-Zapatero, C.; Metz, J. T. Ligand efficiency indices as guideposts for drug discovery. *Drug Discovery Today* **2005**, *10*, 464−469.

(15) Leung, C. S.; Leung, S. S. F.; Tirado-Rives, J.; Jorgensen, W. L. Methyl effects on protein-ligand binding. *J. Med. Chem.* **2012**, *55*, 4489−4500.

(16) Lommerse, J. P. M.; Stone, A. J.; Taylor, R.; Allen, F. H. The nature and geometry of intermolecular interactions between halogens and oxygen or nitrogen. *J. Am. Chem. Soc.* **1996**, *118*, 3108−3116.

(17) Menear, K. A.; Adcock, C.; Boulter, R.; Cockcroft, X. L.; Copsey, L.; Cranston, A.; Dillon, K. J.; Drzewiecki, J.; Garman, S.; Gomez, S.; Javaid, H.; Kerrigan, F.; Knights, C.; Lau, A.; Loh, V. M., Jr.; Matthews, I. T.; Moore, S.; O'Connor, M. J.; Smith, G. C.; Martin, N. M. 4-[3-(4-Cyclopropanecarbonylpiperazine-1-carbonyl)-4-fluoro-benzyl]-2*H*-phthalazin-1-one: a novel bioavailable inhibitor of poly-(ADP-ribose) polymerase-1. *J. Med. Chem.* **2008**, *51*, 6581−6591.

(18) Karlberg, T.; Markova, N.; Johansson, I.; Hammarström, M.; Schütz, P.; Weigelt, J.; Schüler, H. Structural basis for the interaction between tankyrase-2 and a potent Wnt-signaling inhibitor. *J. Med. Chem.* **2010**, *53*, 5352−5355.

(19) Chiang, Y. J.; Hsiao, S. J.; Yver, D.; Cushman, S. W.; Tessarollo, L.; Smith, S.; Hodes, R. J. Tankyrase 1 and tankyrase 2 are essential but redundant for mouse embryonic development. *PLoS One* **2008**, *3*, e2639.

(20) Gunaydin, H.; Gu, Y.; Huang, X. Novel binding mode of a potent and selective tankyrase inhibitor. *PLoS One* **2012**, *7*, e33740.

(21) Murray, C. W.; Rees, D. C. The rise of fragment-based drug discovery. *Nat. Chem.* **2009**, *1*, 187−192.

(22) Wahlberg, E.; Karlberg, T.; Kouznetsova, E.; Markova, N.; Macchiarulo, A.; Thorsell, A.-G.; Pol, E.; Frostell, Å.; Ekblad, T.; Öncü, D.; Kull, B.; Robertson, G. M.; Pellicciari, R.; Schüler, H.; Weigelt, J. Family-wide chemical profiling and structural analysis of PARP and tankyrase inhibitors. *Nat. Biotechnol.* **2012**, *30*, 283−288.

(23) Murray, C. W.; Verdonk, M. L.; Rees, D. C. Experiences in fragment-based drug discovery. *Trends Pharmacol. Sci.* **2012**, *33*, 224−232.

(24) Brameld, K. A.; Kuhn, B.; Reuter, D. C.; Stahl, M. Small molecule conformational preferences derived from crystal structure

data. A medicinal chemistry focused analysis. *J. Chem. Inf. Model.* **2008**, *48*, 1−24.
(25) Black, E.; Breed, J.; Breeze, A. L.; Embrey, K.; Garcia, R.; Gero, T. W.; Godfrey, L.; Kenny, P. W.; Morley, A. D.; Minshull, C. A.; Pannifer, A. D.; Read, J.; Rees, A.; Russell, D. J.; Toader, D.; Tucker, J. Structure-based design of protein tyrosine phosphatase-1B inhibitors. *Bioorg. Med. Chem. Lett.* **2005**, *15*, 2503−2507.
(26) The script is based on the script prepared by Frank Niesen, SGC Oxford (ftp://ftp.sgc.ox.ac.uk/pub/biophysics), adapted to integrate XLFIT (http://www.idbs.com/products-and-services/desktop-and-oem/xlfit-curve-fitting/). Accessed 1 June 2013.
(27) Dong, A.; Xu, X.; Edwards, A. M.; Chang, C.; Chruszcz, M.; Cuff, M.; Cymborowski, M.; Di Leo, R.; Egorova, O.; Evdokimova, E.; Filippova, E.; Gu, J.; Guthrie, J.; Ignatchenko, A.; Joachimiak, A.; Klostermann, N.; Kim, Y.; Korniyenko, Y.; Minor, W.; Que, Q.; Savchenko, A.; Skarina, T.; Tan, K.; Yakunin, A.; Yee, A.; Yim, V.; Zhang, R.; Zheng, H.; Akutsu, M.; Arrowsmith, C.; Avvakumov, G. V.; Bochkarev, A.; Dahlgren, L. G.; Dhe-Paganon, S.; Dimov, S.; Dombrovski, L.; Finerty, P., Jr.; Flodin, S.; Flores, A.; Graslund, S.; Hammerstrom, M.; Herman, M. D.; Hong, B. S.; Hui, R.; Johansson, I.; Liu, Y.; Nilsson, M.; Nedyalkova, L.; Nordlund, P.; Nyman, T.; Min, J.; Ouyang, H.; Park, H. W.; Qi, C.; Rabeh, W.; Shen, L.; Shen, Y.; Sukumard, D.; Tempel, W.; Tong, Y.; Tresagues, L.; Vedadi, M.; Walker, J. R.; Weigelt, J.; Welin, M.; Wu, H.; Xiao, T.; Zeng, H.; Zhu, H. In situ proteolysis for protein crystallization and structure determination. *Nat. Methods* **2007**, *4*, 1019−1021.
(28) Kimple, A. J.; Muller, R. E.; Siderovski, D. P.; Willard, F. S. A capture coupling method for the covalent immobilization of hexahistidine tagged proteins for surface plasmon resonance. *Methods Mol. Biol.* **2010**, *627*, 91−100.
(29) Scrubber2. http://www.biologic.com.au/. Accessed 1 June 2013.
(30) McPhillips, T. M.; McPhillips, S. E.; Chiu, H. J.; Cohen, A. E.; Deacon, A. M.; Ellis, P. J.; Garman, E.; Gonzalez, A.; Sauter, N. K.; Phizackerley, R. P.; Soltis, S. M.; Kuhn, P. Blu-Ice and the Distributed Control System: software for data acquisition and instrument control at macromolecular crystallography beamlines. *J. Synchrotron Radiat.* **2002**, *9*, 401−406.
(31) Otwinowski, Z.; Minor, W. Processing of X-ray diffraction data collected in oscillation mode. In *Macromolecular Crystallography, Part A*; Carter, C. W., Jr., Sweet, R. M., Eds.; Methods in Enzymology, Vol. *276*; Academic Press: New York, 1997; pp 307−326 .
(32) Leslie, A. G. W.; Powell, H. R. *Evolving Methods for Macromolecular Crystallography*; Springer Verlag: Dordrecht, The Netherlands, 2007; Vol. *245*, pp 41−51.
(33) McCoy, A. J.; Grosse-Kunstleve, R. W.; Adams, P. D.; Winn, M. D.; Storoni, L. C.; Read, R. J. Phaser crystallographic software. *J. Appl. Crystallogr.* **2007**, *40*, 658−674.
(34) Winn, M. D.; Ballard, C. C.; Cowtan, K. D.; Dodson, E. J.; Emsley, P.; Evans, P. R.; Keegan, R. M.; Krissinel, E. B.; Leslie, A. G.; McCoy, A.; McNicholas, S. J.; Murshudov, G. N.; Pannu, N. S.; Potterton, E. A.; Powell, H. R.; Read, R. J.; Vagin, A.; Wilson, K. S. Overview of the CCP4 suite and current developments. *Acta Crystallogr., D :Biol. Crystallogr.* **2011**, *67*, 235−242.
(35) Emsley, P.; Cowtan, K. Coot: model-building tools for molecular graphics. *Acta Crystallogr., D: Biol. Crystallogr.* **2004**, *60*, 2126−2132.
(36) Murshudov, G. N.; Vagin, A. A.; Dodson, E. J. Refinement of macromolecular structures by the maximum-likelihood method. *Acta Crystallogr., D: Biol. Crystallogr.* **1997**, *53*, 240−255.
(37) The 3D structure generator CORINA is available from Molecular Networks GmbH, Erlangen, Germany (http://www.molecular-networks.com). Accessed 1 June 2013.
(38) Schrodinger, LLC. *The PyMOL Molecular Graphics System*, version 1.3r1; Portland, OR, 2010.
(39) *Molecular Operating Environment (MOE)*, 2011.10; Chemical Computing Group Inc.: Montreal, Quebec, Canada, 2011.